

## Single-crystal graphene on Ir(110)

Stefan Kraus<sup>1,\*</sup>, Felix Huttmann,<sup>1</sup> Jeison Fischer<sup>1</sup>, Timo Knispel,<sup>1</sup> Ken Bischof,<sup>1</sup> Alexander Herman,<sup>2</sup> Marco Bianchi,<sup>3</sup> Raluca-Maria Stan,<sup>3</sup> Ann Julie Holt,<sup>3</sup> Vasile Caciuc,<sup>4</sup> Shigeru Tsukamoto<sup>4</sup>, Heiko Wende,<sup>2</sup> Philip Hofmann,<sup>3</sup> Nicolae Atodiresei<sup>4,†</sup> and Thomas Michely<sup>1</sup>

<sup>1</sup>*II. Physikalisches Institut, Universität zu Köln, Zùlpicher Straße 77, 50937 Köln, Germany*

<sup>2</sup>*Faculty of Physics and Center for Nanointegration Duisburg-Essen (CENIDE), University of Duisburg-Essen, Lotharstraße 1, 47048 Duisburg, Germany*

<sup>3</sup>*Department of Physics and Astronomy, Interdisciplinary Nanoscience Center (iNANO), Aarhus University, 8000 Aarhus C, Denmark*

<sup>4</sup>*Peter Grünberg Institute and Institute for Advanced Simulation, Forschungszentrum Jùlich, Wilhelm-Johnen-StraÙe, 52428 Jùlich, Germany*



(Received 18 November 2021; revised 19 March 2022; accepted 22 March 2022; published 4 April 2022)

A single-crystal sheet of graphene is synthesized on the low-symmetry substrate Ir(110) by thermal decomposition of C<sub>2</sub>H<sub>4</sub> at 1500 K. Using scanning tunneling microscopy, low-energy electron diffraction, angle-resolved photoemission spectroscopy, and *ab initio* density functional theory, the structure and electronic properties of the adsorbed graphene sheet and its moiré with the substrate are uncovered. The adsorbed graphene layer forms a wave pattern of nanometer wavelength with a corresponding modulation of its electronic properties. This wave pattern is demonstrated in density functional theory calculations to enable the templated adsorption of naphthalene molecules, and in experiment to uniaxially align sandwich-molecular wires composed of Eu and cyclooctatetraene molecules.

DOI: [10.1103/PhysRevB.105.165405](https://doi.org/10.1103/PhysRevB.105.165405)

### I. INTRODUCTION

*In situ* grown graphene (Gr) is an excellent inert substrate for subsequent growth and van der Waals epitaxy. Examples are the growth of EuO(001) on Gr/Ir(111) [1], or the van der Waals epitaxy of transition metal dichalcogenide layers on bilayer Gr/6H-SiC(0001) [2,3] or on Gr/Ir(111) [4,5]. Due to its inertness, Gr is also well suited as a substrate when investigating the properties of molecular layers in the absence of strong molecule-substrate hybridization [6,7]. Similarly, its inertness makes it an ideal substrate for organometallic chemistry with the function to confine the reactant diffusion to two dimensions [8]. In the case of Gr forming a moiré with its growth substrate, templating of molecular layers [9] and of atom or cluster superlattices has also been reported [10,11].

Gr growth also has a substantial effect on its substrate: Step edges are moved [12], step bunches and facets are formed [13,14], or vicinal growth substrates become faceted [15]. A layer of Gr was shown to protect a surface against oxidation, e.g., for Ni(111) [16] or Pt(100) [17], or to prevent the lifting of a reconstruction [18]. Noteworthy, the protection of a metal surface against the formation of a surface reconstruction has not yet been reported.

Up to now, mostly symmetry-matching substrates were used for *in situ* growth of Gr, e.g., fcc(111) or hcp(0001) surfaces [19]. Depending on the strength of interaction between Gr and the substrate, either single-domain Gr could be grown, e.g., for Ru(0001) [20] (good orientation due to strong inter-

action) or multidomain structures result, e.g., for Pt(111) [21] or Cu(111) [22]. For strongly interacting substrates forming a moiré with Gr the corrugation is often substantial due to the spatial variation of binding within the moiré unit cell [23]. Gr/Ir(111) is a unique case, in which the interaction is still weak, but due to proper selection of growth conditions, a well-oriented single-crystal Gr sheet can still be grown [24,25].

Far less work has been conducted regarding the growth of Gr and other two-dimensional materials on non-symmetry-matching substrates of fourfold [17] and twofold symmetry [26–31]. Gr on fcc(110) metal surfaces displays domain formation or multiple orientations. This holds for Ni(110), Cu(110), and Pt(110), irrespective of whether the interaction with the substrate is strong or weak [26–28]. Up to now, among the metals only the quasihexagonal dense-packed bcc(110) surface of Fe, still only of twofold symmetry, was shown to enable Gr growth with unique orientation [29]. Intense research was triggered by the finding that on the (110) face of the semiconductor Ge, growth of large Gr single-crystal layers is possible [30,32], though at the risk of growth close to substrate melting. Also for the isostructural and isoelectric hexagonal boron nitride (h-BN) monolayers, the growth of single-domain phase-pure layers on only twofold-symmetric substrates was not feasible on metals [33–36]. The exception is the growth of h-BN on Pt(110), where the adlayer imposes a complex reconstruction change of the substrate [37].

Here, we introduce Gr on the low-symmetry substrate Ir(110), which displays single-domain single-crystal growth when choosing the proper growth conditions. The perfection by which the Gr layer can be fabricated is surprising, when considering that the clean Ir(110) surface is heavily

\*kraus@ph2.uni-koeln.de (experiment)

†n.atodiresei@fz-juelich.de (theory)

reconstructed at room temperature. Unreconstructed Ir(110) forms a ridge pattern of (331) and (33 $\bar{1}$ ) nanofacets with a corrugation in the nanometer range [38]. Under the Gr cover, however, Ir(110) remains unreconstructed.

Using scanning tunneling microscopy (STM) and low-energy electron diffraction (LEED), the moiré of Gr with Ir(110) is determined. Density functional theory (DFT) calculations reveal a strong modulation of binding and charge transfer to Gr associated with the moiré wave pattern along the [1 $\bar{1}$ 0] direction of the substrate with a periodicity of 10 Å.

The use of this wave pattern for templated adsorption is directly demonstrated here. In DFT calculations, naphthalene is used as a paradigm for an aromatic molecule to explore the anisotropic energy landscape of physisorption induced by the wave pattern. Based on these insights, uniaxial alignment of sandwich-molecular wires during organometallic on-surface synthesis [8,39] is experimentally demonstrated.

## II. METHODS

Gr on Ir(110) was synthesized with identical results on two different crystals in two different ultrahigh-vacuum systems in Cologne, one with a base pressure below  $1 \times 10^{-10}$  mbar and STM imaging at 300 K, and the other with a base pressure of  $3 \times 10^{-10}$  mbar in the preparation chamber and below  $1 \times 10^{-11}$  mbar in the STM chamber where imaging is conducted at 1.7 K. Gases are delivered through a gas dosing tube giving rise to a pressure enhancement by a factor of 80 compared with the pressure measured through a distant ion gauge specified here. Sample cleaning was accomplished by exposure to  $1 \times 10^{-7}$  mbar oxygen at 1200 K when needed, cycles of noble gas sputtering (Ar, Xe), and brief annealing to 1500 K. Closed layers of Gr on Ir(110) were grown by exposure to  $2 \times 10^{-7}$  mbar ethylene for 210 s at 1500 K for the single-domain Gr phase. This type of chemical vapor deposition of Gr on Ir(110) is self-limiting as the dehydrogenation of ethylene ceases when the entire sample is covered by a Gr monolayer, similar to the case with Ir(111) [40]. For the two-domain Gr phase briefly mentioned in this paper and discussed in the Supplemental Material [41], the ethylene exposure was at 1300 K. The Gr quality obtained did not depend on the cooling rate from the growth temperature within the limits given by the different experimental systems. No indication for carbon segregation was found. Sandwich-molecular wires composed of Eu and cyclooctatetraene (Cot) molecules (briefly, EuCot wires) were grown at a sample temperature of 300 K by sublimation of Eu from a Knudsen cell with a deposition rate of  $1.1 \times 10^{17}$  atoms/(m<sup>2</sup> s) at a background pressure of  $1 \times 10^{-8}$  mbar Cot [8]. The software WSXM [42] was used for STM data processing.

To ensure Gr quality and for structural characterization, LEED was used in an energy range of 30–150 eV. The LEED patterns shown are contrast inverted for better visibility.

In Aarhus, samples were prepared *in situ* in an ultrahigh-vacuum chamber (base pressure  $3 \times 10^{-10}$  mbar) using the recipe described above, but with Ne used for sputtering. Angle-resolved photoemission spectroscopy (ARPES) measurements have been conducted at the SGM-3 beam line at the synchrotron ASTRID2, which is connected with the preparation chamber. The samples investigated by ARPES have been

checked *in situ* using the Aarhus STM and LEED mounted at the end station. The samples displayed the same sample morphology, moiré, and diffraction pattern as the samples prepared in Cologne.

Our *ab initio* density functional theory (DFT) [43,44] calculations were carried out using the projector augmented wave method (PAW) [45] as implemented in the Vienna *ab initio* simulation package (VASP) code [46–48]. The van der Waals (vdW) interactions present in the Gr/Ir(110) system were taken into account by employing the nonlocal correlation energy functional vdW-DF2 [49] together with a reoptimized [50] Becke (B86b) exchange energy functional [51]. Gr on Ir(110) was modeled by a slab containing three Ir layers and a vacuum region of  $\approx 21$  Å amounting to 350 C and 264 Ir atoms, respectively. Due to the large supercell size, the Ir slab thickness was limited to three layers for computational feasibility. The bottom Ir layer was fixed, while all other atoms were fully relaxed. Although three Ir layers represent only a simplified model of the Ir substrate, it enables an adequate description of the substrate geometry and the chemical bonding between Gr and the substrate. The ground-state geometry and its electronic structure of this system have been obtained for a kinetic energy cutoff of 500 eV and a threshold value of the calculated Hellmann-Feynman forces of  $\approx 0.005$  eV/Å. Furthermore, for the structural relaxation the Brillouin zone integrations were performed using the  $\Gamma$  point, while the density of states (DOS) was obtained with the help of a  $2 \times 2$  k mesh.

## III. RESULTS AND DISCUSSION

*Superstructure: Experiment.* Gr is grown on carefully cleaned Ir(110) through exposure to ethylene at 1500 K. After cooldown to 300 K, STM finds large flat terraces, separated by plateaus with flat top levels and elongated along the [110] direction. The profile in Fig. 1(a) shows a plateau height of several nanometers. The plateau top level and the surrounding base level are flat. There is no indication of a ridge pattern of (331) and (33 $\bar{1}$ ) nanofacets with a corrugation in the nanometer range [38], as is observed after cooldown in the absence of a Gr cover (compare Fig. S1 in the Supplemental Material [41]). A zoom into a flat terrace area makes a twofold symmetric moiré visible, as shown in Fig. 1(b). We define the rectangular moiré cell as well as the moiré vectors  $\vec{m}_1$  and  $\vec{m}_2$  as indicated in Fig. 1(b). The moiré leads to a well visible wave pattern with wave vector in the direction of  $\vec{m}_2$ , i.e., along the [1 $\bar{1}$ 0] direction. The wave crests and troughs are consequently oriented along the [001] direction. The additional, larger-wavelength periodicity with wave vector in the direction of  $\vec{m}_1$  is less pronounced.

Both periodicities can be recognized in the profile of Fig. 1(b). With the profiles taken on the wave pattern crests and under the tunneling conditions chosen, the corrugation is 0.08 Å for the long-wavelength periodicity with wave vector along  $\vec{m}_1$  [cyan line in Fig. 1(b)], while it is 0.17 Å for the wave pattern with wave vector along  $\vec{m}_2$  [blue line in Fig. 1(b)]. It can be seen in Fig. 1(b) that on some wave crests an additional corrugation with a wavelength of about  $\frac{1}{4}$  of the moiré periodicity is present. By visually analyzing this extra corrugation along the wave crests highlighted by black arrows

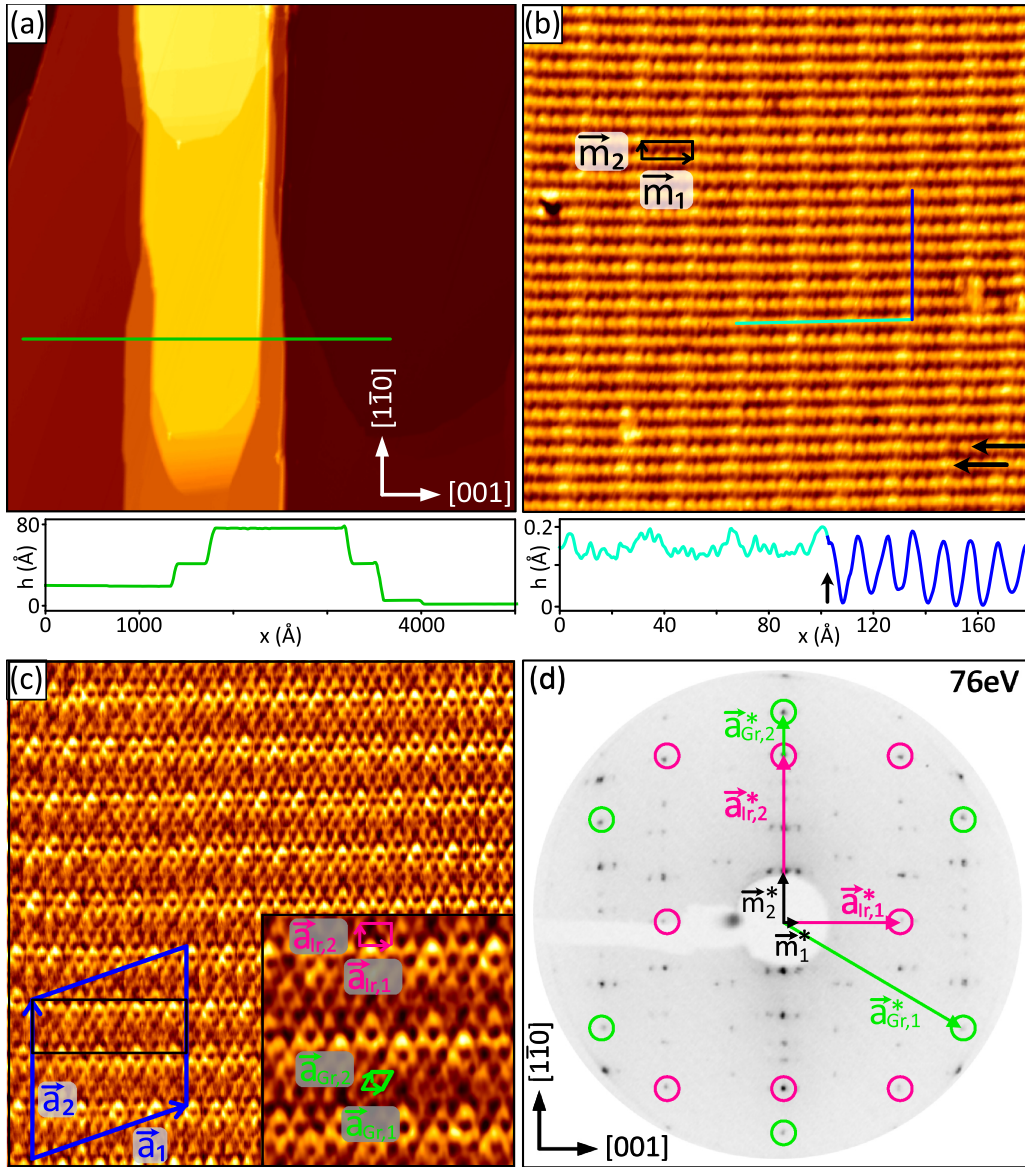


FIG. 1. (a) Large-scale STM topograph ( $7000 \times 7000 \text{ \AA}^2$ ) of Gr/Ir(110) grown at  $T = 1500 \text{ K}$ . The  $[001]$  and  $[1\bar{1}0]$  directions specified in the lower right corner are valid also for (b), (c), and (d). The STM height profile along the green line is shown below the topograph. (b) STM topograph ( $300 \times 300 \text{ \AA}^2$ ) of flat terrace area. The black rectangle indicates the moiré unit cell. Black arrows highlight the varying appearance of wave crests. The STM height profile along the path of the cyan and blue lines is shown below the topograph. A small black arrow in this height profile plot marks the location where the profile changes from the  $[001]$  to  $[1\bar{1}0]$  direction. (c) Atomic resolution STM topograph ( $100 \times 100 \text{ \AA}^2$ ) with commensurate superstructure cell and primitive translations  $\vec{a}_1$  and  $\vec{a}_2$  indicated by the blue rhomboid. The moiré unit cell is shown with a black rectangle. Inset: magnified view ( $30 \times 30 \text{ \AA}^2$ ) with centers of Gr rings visible as dark depressions. Gr and Ir(110) unit cells and primitive translations are indicated. (d) 76-eV LEED pattern of Gr/Ir(110). First-order Ir and Gr reflections are encircled in magenta and green, respectively. Reciprocal moiré, Gr, and Ir primitive translations are indicated. See text. STM imaging temperatures are 300 K in (a) and (b) and 1.7 K in (c). Tunneling parameters are (a)  $U_{\text{bias}} = -1.33 \text{ V}$  and  $I_t = 0.8 \text{ nA}$ , (b)  $U_{\text{bias}} = -1.33 \text{ V}$  and  $I_t = 1.1 \text{ nA}$ , and (c)  $U_{\text{bias}} = -0.05 \text{ V}$  and  $I_t = 20.0 \text{ nA}$ .

in Fig. 1(b) it is obvious that (i) this extra corrugation varies along the wave crests and (ii) neighboring wave crests differ in the amplitude of this corrugation, being almost absent or quite pronounced. While observation (i) suggests the presence of small tilts in the orientation of the two lattices, observation (ii) indicates that the moiré is not commensurate along  $\vec{m}_2$ . The large-wavelength periodicity with wave vector in the direction of  $\vec{m}_1$  is also not perfectly uniform and is affected by the presence of defects. This is apparent for the vertical crests at the

right of Fig. 1(b), where the crests slightly change orientation due to the defect in the middle right of the topograph. Again, this indicates the presence of small tilts and shears of the Gr lattice.

We note that depending on the tunneling parameters and tip condition, the corrugation may differ substantially from the apparent corrugation found for the topograph of Fig. 1(b). Corrugations of up to  $0.4 \text{ \AA}$  for the long-wavelength periodicity with wave vector along  $\vec{m}_1$  and up to  $0.8 \text{ \AA}$  for the wave

pattern with wave vector along  $\vec{m}_2$  are found. The corrugation along  $\vec{m}_1$  is generally found to be smaller than the one along  $\vec{m}_2$ . Elastic effects of tip-surface interaction at very low tunneling resistances, and at somewhat larger resistances a distance dependence of the corrugation on the local density of states are most likely the origin of this variation.

In the atomically resolved STM topograph of Fig. 1(c), the centers of the Gr honeycombs are well visible as dark depressions. The Gr zigzag rows are close to perfectly aligned with the [001] direction. The moiré periodicity  $m_2$  along the [1 $\bar{1}$ 0] direction is well visible and caused by the superposition of the 2.715-Å periodicity of Ir(110) and the zigzag row spacing of Gr. Application of the moiré construction for the case of aligned periodicities as outlined in Ref. [52] results in  $m_2 = (9.94 \pm 0.15)$  Å and a zigzag row spacing of  $(2.133 \pm 0.007)$  Å. This row spacing implies a Gr lattice parameter of  $a_{\text{Gr}} = (2.463 \pm 0.008)$  Å. The Gr lattice parameter agrees within the limits of error with the in-plane lattice parameter of relaxed graphite  $a_{\text{graphite}} = 2.4612$  Å [53]. Gr on Ir(110) appears to be unstrained. The determination of the periodicity  $m_1$  is more difficult, since it is not clearly visible in the atomically resolved topograph of Fig. 1(c) and similar ones, presumably due to the low-tunneling-resistance conditions needed to obtain atomic resolution. However, the observation of the ratio of  $m_1$  to  $m_2$  is possible in STM topographs without atomic resolution and allows one to estimate  $m_1 = (33 \pm 2)$  Å. Finally, the Fourier transform of Fig. 1(c) displays spots corresponding to the Ir(110) and Gr lattices simultaneously (compare Fig. S2 in the Supplemental Material [41]). Its analysis confirms the absence of significant strain in Gr and the magnitude of the Gr primitive translations  $\vec{a}_{\text{Gr},1}$  and  $\vec{a}_{\text{Gr},2}$  to deviate less than 0.5%.

The LEED pattern of Gr/Ir(110) shown in Fig. 1(d) can be decomposed into reflections of *unreconstructed* Ir(110), encircled in magenta, and first-order reflections of a single Gr domain, encircled in green. All other reflections are linear combinations of the Ir(110) and Gr reciprocal lattice vectors. The moiré periodicity along [001] corresponds to the difference  $\vec{m}_1^* = 2 \cdot \vec{a}_{\text{Gr},1}^* + \vec{a}_{\text{Gr},2}^* - 3 \cdot \vec{a}_{\text{Ir},1}^*$ , and that along [1 $\bar{1}$ 0] corresponds to  $\vec{m}_2^* = \vec{a}_{\text{Gr},2}^* - \vec{a}_{\text{Ir},2}^*$ . The vectors  $\vec{m}_i^*$ ,  $\vec{a}_{\text{Gr},i}^*$ , and  $\vec{a}_{\text{Ir},i}^*$  indicated in Fig. 1(d) are the reciprocal vectors to  $\vec{m}_i$ ,  $\vec{a}_{\text{Gr},i}$ , and  $\vec{a}_{\text{Ir},i}$  [compare Figs. 1(b) and 1(c)]. The moiré periodicities derived from LEED are  $m_1 = (31 \pm 2)$  Å and  $m_2 = (9.8 \pm 0.3)$  Å. They agree, within the limits of error, well with our STM analysis. The same holds for the real-space Gr lattice parameter  $a_{\text{Gr}} = (2.49 \pm 0.04)$  Å derived from the LEED pattern.

Since the spot size of the primary electron beam on the sample is of the order of 1 mm, the single-domain character of Gr is macroscopic. Also when the sample is moved laterally under the electron beam of the LEED setup, no change in the LEED pattern is observed. STM conducted at various locations on the sample invariably detects the moiré over the entire scan field consistent with the absence of holes in the Gr layer and the monolayer character of Gr. The Gr layer is found to be continuous over steps and step bunches (compare also the Discussion section below). Taken together, Gr on Ir(110) is a two-dimensional (2D) single crystal on the Ir(110) sample surface.

On a side note, we also observed the formation of a two-domain Gr phase, but at a lower growth temperature of 1300 K. Mixtures of the two phases emerge for intermediate temperatures. Compare Fig. S3 in the Supplemental Material [41] for a large-scale STM topograph, a LEED pattern, and a structural model of the low-temperature phase. It should be noted that phase-pure single-domain Gr growth is impeded when graphene islands are allowed to form already at temperatures well below 1500 K. This may be the case when the temperature of the Ir(110) crystal is ramped up in a poor background pressure with carbon-containing molecules that are decomposed on the hot Ir surface, or when the gas used for chemical vapor deposition growth is admitted already before the temperature of 1500 K is reached. Presumably, the low-temperature Gr phase islands grown during temperature ramp-up do not (or not all) reorient during subsequent growth at 1500 K impeding a phase-pure sample.

Summarizing our analysis, STM and LEED suggest an incommensurate moiré of unstrained or marginally strained Gr with Ir(110). In fact, assuming unstrained Gr with its graphite lattice parameter  $a_{\text{graphite}} = 2.4612$  Å and the zigzag rows parallel to the [001] direction, as observed in STM and LEED, would result in  $m_1 = 32.02$  Å and  $m_2 = 9.91$  Å. These numbers agree very well with our STM and LEED analysis. In order to be able to conduct DFT calculations, we need to approximate the experimental situation through a commensurate superstructure cell. The smallest commensurate unit cell with negligible Gr strain is indicated as a blue rhomboid in Fig. 1(c) and in the ball model of Fig. 2(a). The unit cell is spanned by the primitive translations  $\vec{a}_1$  and  $\vec{a}_2$  of lengths  $a_1 = 32.58$  Å and  $a_2 = 29.87$  Å. The triple length of  $\vec{a}_2$  compared with  $\vec{m}_2$  takes into account that along the [1 $\bar{1}$ 0] direction, approximate commensurability is only achieved after three moiré periods  $m_2$ . In matrix notation the commensurate superstructure can be expressed as  $\begin{pmatrix} 8 & 4 \\ 0 & 11 \end{pmatrix}$  with respect to

Ir(110) and  $\begin{pmatrix} 10 & 5 \\ -7 & 14 \end{pmatrix}$  with respect to Gr (compare Fig. S4 in the Supplemental Material [41]). The Gr lattice parameters  $a_{\text{Gr},1} = 2.457$  Å and  $a_{\text{Gr},2} = 2.463$  Å in the commensurate superstructure unit cell are close to the in-plane lattice parameters of relaxed graphite  $a_{\text{graphite}} = 2.4612$  Å [53] and to our measurements. They are only slightly compressed by 0.17% or stretched by 0.07% with respect to  $a_{\text{graphite}}$ .

*Superstructure: Ab initio calculations.* For our DFT calculations we used a slab consisting of three layers of Ir, the Gr layer, and 21 Å of vacuum in the  $z$  direction. The DFT supercell shown in Fig. 2(a) is based on the superstructure unit cell defined by  $\vec{a}_1$  and  $\vec{a}_2$  [compare Fig. 1(c)].

The adsorption energy per C atom amounts to  $E_{\text{ads}} = -140.2$  meV, about twice the value obtained for Gr/Ir(111) with the same exchange-correlation functional [54]. Side views of the supercell are presented in Fig. 2(b) with the direction of view along [001], normal to the dense-packed Ir rows and along a Gr zigzag direction, and Fig. 2(c) with the direction of view along [1 $\bar{1}$ 0], i.e., along the dense-packed Ir rows and a Gr armchair direction. The view along [001] displays a clear wave pattern of the Gr layer with wave vector along the direction of  $\vec{a}_2$  or the [1 $\bar{1}$ 0] direction. The wave

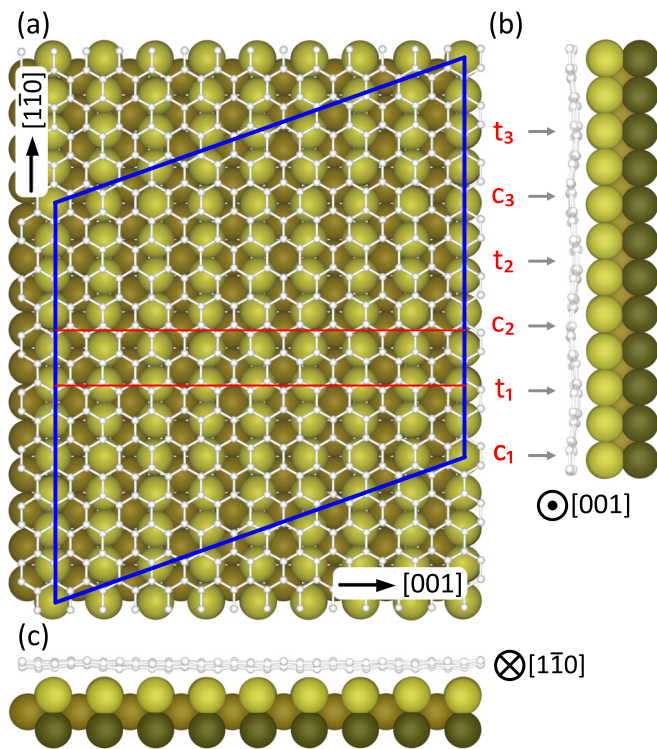


FIG. 2. Ball model representations of relaxed DFT geometries for Gr/Ir(110). Ir atoms, light (top layer) to dark (bottom layer) brown spheres; C atoms, small light gray spheres connected by light gray lines. (a) Top view with DFT supercell indicated by the blue rhomboid. The  $[1\bar{1}0]$  and  $[001]$  directions are also shown. (b) Side view with the  $[001]$  direction out of the drawing plane as indicated. A pattern of crests  $c_1$ – $c_3$  and troughs  $t_1$ – $t_3$  in the Gr layer is visible along  $[1\bar{1}0]$  with their positions highlighted by arrows. (c) Side view with the  $[1\bar{1}0]$  direction into the drawing plane as indicated.

crests are labeled  $c_1$ ,  $c_2$ , and  $c_3$ , and the wave troughs are labeled  $t_1$ ,  $t_2$ , and  $t_3$ . Close inspection reveals that the three wave crests and the three wave troughs are not equivalent in symmetry: While a zigzag row is either precisely aligned to an Ir-atom row along  $[001]$  for  $t_1$  or precisely aligned between two Ir-atom rows for  $c_2$ , this alignment is only approximate for the other two crests and troughs. Consequently, the corrugation of the wave pattern is nonuniform ranging from 0.32 to 0.46 Å. The view along  $[1\bar{1}0]$  displays no clear corrugation pattern of the Gr layer.

These DFT results are in good agreement with the experimental observation of a pronounced wave pattern with crests along  $[001]$  with the same periodicity as in DFT. The experimental corrugation of this wave pattern [blue in the height profile of Fig. 1(b)] is generally larger than the corrugation in the direction normal to it [cyan in the height profile of Fig. 1(b)], again in qualitative agreement with our DFT calculation. The DFT-calculated corrugation of up to 0.46 Å is well within the range of experimentally measured corrugations of 0.15–0.8 Å along the  $[1\bar{1}0]$  direction.

**Binding: *Ab initio* calculations.** Already the side views of Figs. 2(b) and 2(c) suggest that the binding configurations of the C atoms to the Ir(110) substrate vary substantially. On a global level this is evident by noting that the C-Ir bond length,

i.e., the distance between a C atom of Gr and the nearest Ir substrate atom, varies between 2.11 and 3.10 Å, i.e., from a strong chemisorption to a weak chemisorption bond length. This large variation is primarily caused by the large corrugation of the Ir substrate with its hill-and-valley structure. A manifestation of the binding heterogeneity is the Gr wave pattern as apparent in the side view of Fig. 2(b). To obtain insight into the underlying physics and associated wavelike variation of Gr's properties, charge density difference plots along the red lines in Fig. 2(a) in the trough  $t_1$  and the crest  $c_2$  are compared in Figs. 3(a) and 3(b), respectively. In the cut through the trough  $t_1$  shown in Fig. 3(a), charge accumulation (red) between the Ir and the C atoms signals the formation of chemical bonds. These chemical bonds to the substrate cause the C atoms of Gr to acquire partial  $sp^3$  character. Moreover, charge accumulates in the  $\pi$  system above the C-atom plane. In the cut through the crest  $c_2$  shown in Fig. 3(b), essentially no charge accumulation between the C atoms and the distant Ir atoms is present—the chemical bonds are weak. Therefore, in contrast to the troughs, in the crests little charge is injected into the  $\pi$  system above the C atoms. Besides a variation in local work function, the variation of the local charge transfer into the Gr  $\pi$  system implies also a variation of the van der Waals interactions of the Gr layer with physisorbed species. As outlined in Ref. [55], the strength of the van der Waals interactions is larger where the charge cloud of the  $\pi$  system spreads out into the vacuum farther away from the C nuclei. The modulation of the binding character and electronic properties with the wave pattern is also apparent in Fig. 3(c), which shows the charge density difference average over the entire superstructure unit cell and projected onto a plane along the  $[1\bar{1}0]$  direction. There, the variation of binding character and charge donation to the Gr  $\pi$  system is well visible through the variation of strong charge accumulation above and below the C-atom plane.

The charge density difference plots normal to the wave pattern along the Gr armchair direction ( $[1\bar{1}0]$  direction of the Ir substrate) also display a variation of electronic properties. However, on all cuts the dominant wave pattern is superimposed, causing a considerable heterogeneity along the direction of the cut. Compare also Fig. S5 in the Supplemental Material [41].

**Electronic structure of Gr on Ir(110).** Figure 4(a) compares the characteristic V-shaped freestanding Gr density of states (red line) with the Gr partial DOS when adsorbed to Ir(110) (black line). The V shape of the freestanding Gr DOS signals electronically intact Gr with a Dirac cone formed by the Gr  $\pi$  and  $\pi^*$  bands that touch at the Dirac point, where the DOS vanishes. This feature is characteristic for freestanding or physisorbed Gr layers and corresponds to an  $sp^2$  hybridization of its electronic states. The absence of this feature and the substantial partial Gr DOS of Gr/Ir(110) in the entire energy range of a few eV around the Fermi energy signifies considerable modification of the Gr electronic structure when adsorbed to Ir(110), similar, e.g., to the case of Gr on Ni(111) [56]. The diversity of C-Ir bonds noticed already in Fig. 2 gives rise to a diversity of C-Ir hybridizations, which together with the variation of the local charge transfer visible in Fig. 3 gives rise to the smeared-out partial DOS of Gr. The blue curve in Fig. 4(a) represents the partial Gr DOS projected

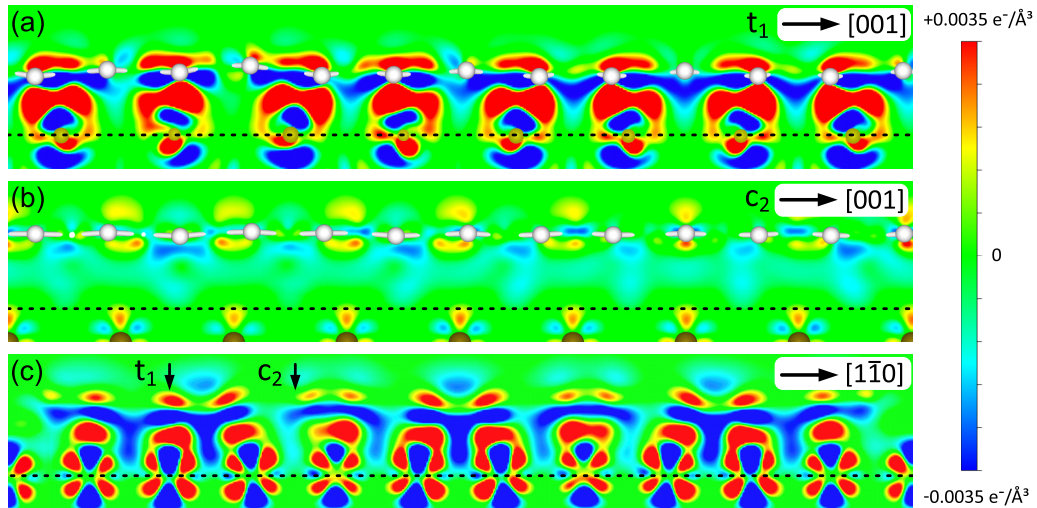


FIG. 3. (a) and (b) Charge density difference plots in the (a) trough and (b) crest locations indicated in Fig. 2(b) as  $t_1$  and  $c_2$  and in Fig. 2(a) by horizontal red lines. (c) Charge density difference average over the entire superstructure unit cell and projected onto a plane along the  $[1\bar{1}0]$  direction corresponding to the view of Fig. 2(b). The positions of the cuts along  $t_1$  and  $c_2$  are indicated by arrows. The black dashed lines indicate the position of the top-level Ir atoms. See text. The color scale for all plots ranges from charge accumulation in red ( $+0.0035$  electrons/ $\text{\AA}^3$ ) to charge depletion in blue ( $-0.0035$  electrons/ $\text{\AA}^3$ ).

onto the carbon  $p_z$  atomiclike orbitals that originally form the Gr  $\pi$  system. The difference between this projection and the entire partial Gr DOS is small but indicates a non-negligible  $sp^3$  character of bonding due to the local chemical interactions between the corrugated Gr and Ir(110) as depicted in Fig. 3.

The electronic structure of the adsorption system has been investigated by ARPES [57]. Figure 4(b) shows the photoemission intensity as a function of binding energy and  $k_{\parallel}$  in the  $\Gamma$ - $K$  direction of the Gr Brillouin zone. The ARPES data show no sign of a Dirac cone or any feature that could be related to the Gr  $\pi$  band down to 5 eV below the Fermi edge. The absence of Gr-related bands in ARPES from Gr/Ir(110) is surprising, as traces of the  $\pi$  band or of the Dirac cone can usually be seen in other strongly hybridized Gr/metal systems in this energy range, though these traces can be weak [58–60]. The detailed data, presented in Figs. S6 and S7 as

well as movies M1 and M2 in the Supplemental Material [41], were taken at three different photon energies to underline the absence of Gr-related features in ARPES of Gr/Ir(110). This absence is fully consistent with the DFT calculations that display no indication of a linear DOS, the hallmark of a Gr Dirac cone. We note that future investigations may find indications of the  $\sigma$  and even the  $\pi$  bands at energies below those investigated here. However, such investigations are beyond the topic and scope of this paper.

*A naphthalene molecule as a sensor for the energy landscape of adsorption on Gr/Ir(110).* To obtain insight into whether the modulation associated with the wave pattern of Gr/Ir(110) can be used to template molecular adsorption, a naphthalene molecule was employed as a sensor in DFT calculations of still feasible computational effort. Using different starting configurations for  $C_{10}H_8$  adsorbed to the crest  $c_2$  and

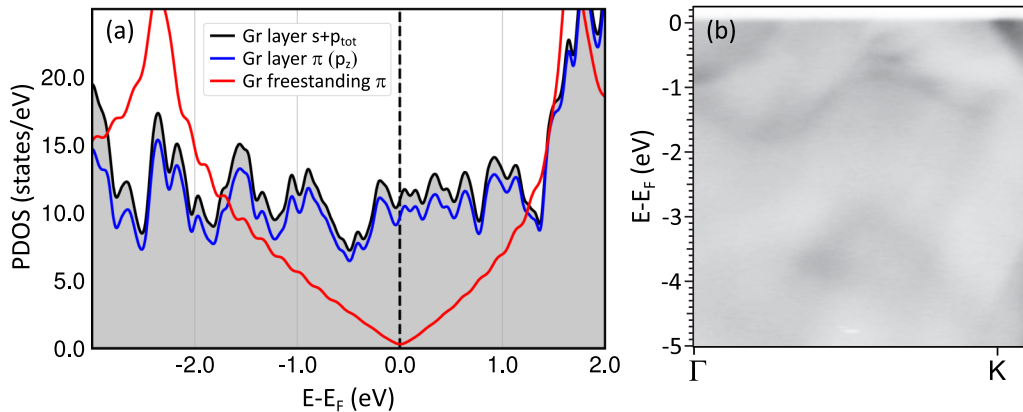


FIG. 4. (a) Red line, density of states (DOS) of freestanding Gr; black line and gray-shaded area, Gr partial DOS (PDOS) when on Ir(110); blue line, Gr partial DOS projected on the Gr  $\pi$  system consisting of  $p_z$  atomiclike orbitals. See text. (b) Angle-resolved photoemission spectrum along  $\Gamma$ - $K$ , recorded at a photon energy of 100 eV and a temperature of  $T = 35$  K. There is no Dirac cone at the  $K$  point, and there are no features that could be related to the Gr  $\pi$  bands in agreement with the DFT calculations.

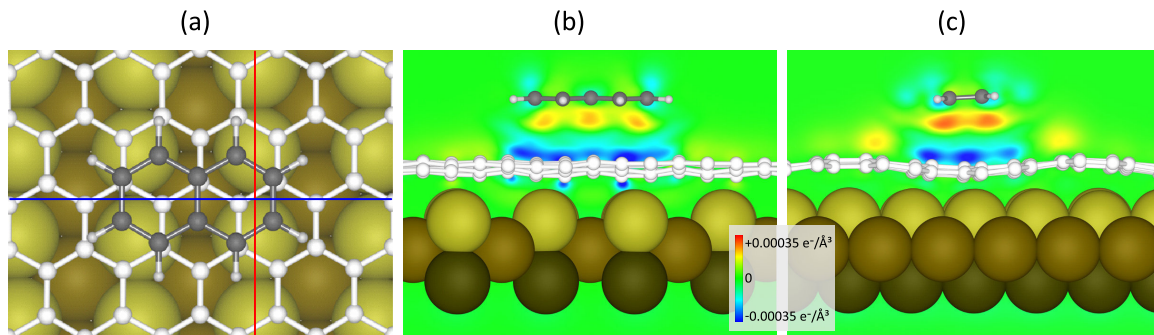


FIG. 5. (a) Top-view ball model for the minimum energy adsorption geometry of  $C_{10}H_8$  in trough  $t_1$  on Gr/Ir(110) (compare Fig. 2). (b) Charge density difference plot along the blue line in (a) of the combined system compared with the sum of the isolated  $C_{10}H_8$  molecule and Gr/Ir(110). (c) Same as (b), but along the red line in (a). The color scale in (b) and (c) is the same as in Fig. 3, but used for one order of magnitude smaller charge density differences ranging from  $+0.00035$  electrons/ $\text{\AA}^3$  for charge accumulation in red to  $-0.00035$  electrons/ $\text{\AA}^3$  for charge depletion in blue.

trough  $t_1$  of Gr/Ir(110) (compare Fig. 2), several local minima of adsorption energy were identified.

Figure 5(a) displays the minimum energy adsorption geometry, where the molecule resides in the trough, as is also obvious from the side-view cuts of the charge density difference plots in Figs. 5(b) and 5(c). Adsorption takes place with the long molecular axis along the trough. No energy minimum could be found for the molecule in different orientations, e.g., with the long axis normal to the trough. The adsorption energy  $E_{\text{ads}}$  is  $-947$  meV, lower by 168 meV compared with the best-bound configuration on a crest. The minimum energy adsorption site in the trough corresponds to the locations where the charge accumulation above Gr is highest (compare Fig. 3). Thus these results are in qualitative agreement with experiments and DFT calculations for naphthalene adsorbed to Gr/Ir(111) [55], where the strength of the van der Waals interactions was found to increase with the charge donated to Gr ( $n$  doping). For the minimum energy configuration shown in Fig. 5, the average naphthalene-graphene distance is  $3.27$  Å, a distance typical for a physisorbed molecule, while for all other local adsorption energy minima the distances are larger. Compare Fig. S8 and Table S1 in the Supplemental Material [41] for additional calculations and more details.

Our calculations make plain that despite Gr's strong interaction with the Ir(110) substrate, it is still an inert substrate for molecular adsorption, acting as a spacer effectively separating the metal from the molecule. The situation is not unexpected, when considering that other "strongly" interacting Gr layers also act as an inert spacer between molecules and the underlying metal. To give an example, the peak desorption temperature of benzene from strongly interacting Gr on Ru(0001) [19] is within the limits of error identical to the one from graphite [61].

*Use of Gr/Ir(110) as a nanotemplate for alignment in on-surface synthesis.* Our theoretical calculations for  $C_{10}H_8$  adsorbed to Gr/Ir(110) imply that this substrate displays an anisotropic physisorption energy landscape and is thereby able to template adsorption and to impose uniaxial alignment. Here, we use the example of on-surface synthesis of sandwich-molecular wires to demonstrate these properties. A sandwich-molecular wire is an organometallic compound consisting of an alternation of metal atoms with ring-shaped

aromatic molecules [62,63]. When Eu atoms and cyclooctatetraene (Cot,  $C_8H_8$ ) molecules (eight-membered carbon rings) are combined in room temperature on-surface synthesis on Gr/Ir(111), Eu is evaporated onto the substrate at a background pressure of Cot, of which the excess reevaporates at 300 K [8]. Because of van der Waals interaction between the wires, they interlock and form monolayer-high islands. On Gr/Ir(111) the islands of parallel wires are *randomly* oriented resulting in diffraction rings rather than spots in LEED [8,39]. The lack of island orientation was found not to depend on coverage. Compare Fig. S9 in the Supplemental Material [41] for an example STM topograph and LEED pattern of EuCot sandwich-molecular wires on Gr/Ir(111). The properties of EuCot wires were already characterized in detail through density functional theory calculations [8,64–66].

As is obvious from Fig. 6, successful on-surface synthesis of EuCot is also possible on Gr/Ir(110). This observation implies directly the mobility of reaction intermediates to wire ends and the reevaporation of the Cot excess at room temperature. This underpins the inertness of the Gr/Ir(110) substrate and the physisorbed state of the unreacted molecules.

In contrast to the random orientation of the wire carpet islands on Gr/Ir(111), growth on the anisotropic Gr/Ir(110) substrate gives rise to thin and long wire islands all oriented along the [001] direction as visible in Fig. 6(a). For larger coverages a well-oriented, coalesced monolayer results, as shown in Fig. 6(b). It is worth noting that wires are oriented along [001], i.e., along the troughs of the moiré, rather than along  $[1\bar{1}0]$ , i.e., along the direction where unreconstructed Ir(110) presents its troughs.

Only step bunches along  $[1\bar{1}0]$ , as visible in Fig. 1(a), cause a deviation from the global [001] wire alignment in their immediate vicinity. They reorient the wires into the bunch direction, typically the  $[1\bar{1}0]$  direction, in a strip width of up to 250 Å. A misoriented patch next to a bunch is visible in the lower right of Fig. 6(b). Compare Fig. S10 in the Supplemental Material [41] for a large-scale STM topograph visualizing the EuCot wire distribution next to a step bunch.

Figure 6(c) displays the corresponding LEED pattern. It exhibits clear diffraction spots of the wire lattice encircled by dashed blue lines. The rhomboidal reciprocal unit cell is indicated in green. Because LEED is a spatial averaging

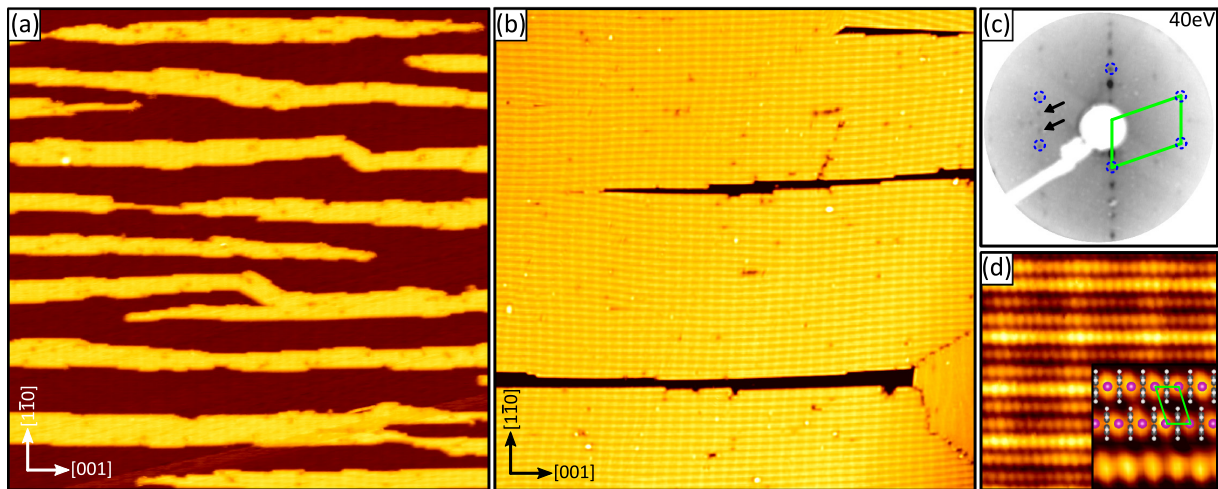


FIG. 6. (a) and (b) STM topographs ( $1500 \times 1500 \text{ \AA}^2$ ) of (a) elongated EuCot wire carpet islands and (b) a full layer on Gr/Ir(110) oriented along the [001] direction. (c) 40-eV LEED pattern of the same sample as in (b). The unit cell of the EuCot wire carpet is indicated by the green rhomboid, with the corresponding first-order reflections encircled by dashed blue lines.  $3 \times 1$  superstructure reflections are highlighted by black arrows. (d) STM topograph ( $100 \times 100 \text{ \AA}^2$ ) of EuCot/Gr/Ir(110) with a  $3 \times 1$  intensity variation along the  $[1\bar{1}0]$  direction resulting from the lattice mismatch of the substrate moiré and the wire carpet. Inset: molecular resolution STM topograph ( $25 \times 25 \text{ \AA}^2$ ) overlaid with a wire model. Magenta dots, Eu atoms; white and black dots, H atoms and C atoms of Cot. The wire carpet unit cell is indicated as a green rhomboid. STM topographs were taken at 300 K. Tunneling parameters are (a)  $U_{\text{bias}} = -2.0 \text{ V}$  and  $I_t = 0.03 \text{ nA}$ , (b)  $U_{\text{bias}} = -1.74 \text{ V}$  and  $I_t = 0.08 \text{ nA}$ , and (d)  $U_{\text{bias}} = -1.82 \text{ V}$  and  $I_t = 0.35 \text{ nA}$ .

technique, the diffraction pattern implies a global alignment of the wires along the [001] direction. Highlighted by the two black arrows in Fig. 6(c),  $3 \times 1$  superstructure reflections can be identified in the direction normal to the wires, of which the origin is explained below. In the molecular resolution STM topograph of Fig. 6(d) the parallel wires are shown together with a ball model overlay of the molecular structure and the wire lattice unit cell. Close inspection of the STM topograph reveals a beating of the wire height (brightness) along  $[1\bar{1}0]$ , where about every third wire appears to be higher. It is this height variation of the wires that gives rise to the  $3 \times 1$  superstructure spots in LEED, which is thus a global feature of wire ordering. The intensity variation can be explained by the mismatch of the interwire distance and the moiré periodicity of the underlying substrate in this direction. Based on the crest spacing of  $\approx 10 \text{ \AA}$  and the wire spacing of  $\approx 6.8 \text{ \AA}$  measured on Gr/Ir(111) [8], three wires fit on two moiré periodicities along  $\bar{m}_2$ . Apparently, two-thirds of the wires are located close to the trough positions, while one-third is located close to a crest position. Furthermore, faint vertical lines of brighter contrast spaced by  $m_1$  reflect the bending of the horizontally aligned wires over the moiré periodicity along [001].

Based on the successful on-surface synthesis using the same parameters as for EuCot wire growth on Gr/Ir(111) [8,39], it is evident that also on Gr/Ir(110) the wires are bound through van der Waals interactions to the substrate. The upright-standing aromatic Cot dianions are in contact with Gr only through their peripheral H atoms. Bound to the cyclic carbon ring, they are unable to interact chemically with Gr. For a single wire, our DFT calculation shown above suggests adsorption to a trough location, where the van der Waals interaction is stronger than on the crests. However, due to substantial interwire van der Waals interaction, single wires are not realized even for smaller coverages. Nevertheless, con-

sistent with a preferential binding to the troughs, two-thirds of the wires are adsorbed close to the troughs rather than to the crests, as noticed above when discussing the  $3 \times 1$  wire superstructure.

Elastic energy considerations are also in favor of adsorption along the wave pattern, i.e., the [001] direction, rather than vertically to the wave pattern. In order to maximize the binding to the substrate, the wires need to adhere conformally to the Gr sheet at an optimum distance defined by Pauli repulsion and van der Waals interactions. For a 1D wire oriented perpendicular to the wave pattern along the  $[1\bar{1}0]$  direction this would imply substantially more bending with shorter periodicity to conform to the wave pattern than for a wire oriented along the [001] direction with substantially less corrugation and larger periodicity  $m_1$ . Thus the elastic energy penalty for wire orientation along the [001] direction is lower, also favoring its orientation along this direction.

It is remarkable that physisorbed species—the 1D sandwich-molecular wires—are perfectly oriented through the Gr/Ir(110) template at temperatures as high as room temperature. However, even if the charge modulation and elastic energy effects are presumably small per formula unit—possibly as low as 10 meV—the wires are composed of hundreds of formula units. Thereby, energy differences for wires adsorbed in different orientations and at different adsorption sites become large.

*Discussion.* Instead of forming the nanofacet reconstruction, Ir(110) remains unreconstructed upon cooldown to room temperature when Gr has been grown on it at 1500 K. To explain this remarkable observation, we note that the surface reconstructions of Ir(110) are driven by the temperature-dependent minimization of surface free energy  $\gamma$ , which itself is linked to the surface stress [67]. The Ir(110) surface was shown to run through a sequence of reconstructions upon

cooling with a  $(2 \times 1)$  missing row reconstruction being present at 800–900 K and a  $(3 \times 1)$  missing row reconstruction being dominant at 500–600 K, while eventually upon cooling the  $(331)/(3\bar{3}1)$  nanofacet reconstruction forms [68,69]. The surface structure of Ir(110) at the Gr growth temperature of 1500 K is unknown, but based on the results for the same surface orientation of the parent element Pt [70], at 1500 K Ir(110) is presumably above the roughening temperature and will display fast surface profile fluctuations due to high mobility. Knowing that a Gr membrane replicates the surface morphology at the growth temperature [13], the morphology observed at 300 K by STM is close to the morphology at the end of growth at 1500 K. Therefore we tentatively conclude that Gr grows on unreconstructed Ir(110). The calculated binding energy of 140.2 meV per C atom is of similar magnitude to the Ir surface free energy, which can be estimated to be of the order of 300 meV for Ir(110) if normalized to the Gr atomic density [71]. It is therefore plausible that upon cooling, reconstructions that lower the surface energy in the clean case are suppressed as they would diminish the adhesion between Gr and the Ir(110) substrate. In fact, any of the known Ir(110) reconstructions make the surface rougher and thus either would reduce the number of binding substrate atoms or would force large deformations in Gr to conform to the substrate. In a brief and somewhat coarse description, the adhering Gr layer shifts the binding of Ir(110) surface atoms to a more bulklike situation due to the formation of Ir-C bonds, largely relieving the driving force for surface reconstruction.

Gr on Ir(110) is a single crystal, if grown at 1500 K, while two domains are found for growth at 1300 K (compare Fig. S3 in the Supplemental Material [41]). The situation is similar for the growth of Gr on Ir(111), where upon increasing the growth temperature the situation changes from multiple domain orientations to a single crystal of Gr [24,25]. Gr on Ir(111) is continuous over steps [40], and so is Gr on Ir(110). Since the EuCot wire synthesis requires an inert substrate, the presence of EuCot wires at and in step bunches directly confirms the continuity of Gr over step bunches. Compare Fig. S11 in the Supplemental Material [41]. The lack of strain in the  $\begin{pmatrix} 8 & 4 \\ 0 & 11 \end{pmatrix}$  commensurate approximation of the high-temperature superstructure suggests that in fact the low-temperature two-domain structure, which is considerably strained (compare Fig. S3 in the Supplemental Material [41] and related discussion), reflects kinetic limitations of the Gr growth process rather than a change in the orientation-dependent adsorption energy. To substantiate such speculations, systematic growth-temperature-dependent studies would be necessary, which are beyond the scope of this work. Nevertheless, we speculate that if the growth temperature can be raised sufficiently, single-crystal Gr layers could be grown also on other fcc(110) surfaces.

Lastly, one might ask why Gr on Ir(110) is so different from Gr on Ir(111), with a much higher binding energy and an electronic structure lacking a Dirac cone. As a first remark it should be noted that although the binding energy of graphene to Ir(110) is 140.2 meV per C atom, much larger than the 69 meV per C atom for the binding energy of graphene to Ir(111) [54], it is still much lower than typical chemisorption energies of several eV per molecule or the 7.6 eV cohesive

energy of Gr [72]. The binding energy of Gr to Ir(110) is comparable to the binding energy of Gr to Ni(111) [73], which is considered as weak chemisorption [74]. We also note that the electronic structure of Gr is especially sensitive to the environment because of the low density of states close to the Dirac point. Therefore a loss of the Dirac cone, as also observed for Ni(111) [56] does not imply a loss of the predominant  $sp^2$  bonding character, as is obvious from the projected DOS in Fig. 4.

Compared with Ir(111), which is smooth and where all surface atoms are ninefold coordinated, Ir(110) is a more open and a corrugated surface, with the surface atoms in the protruding rows being only sixfold coordinated, whereas the surface atoms in the troughs are 1.36 Å below the level of the row atoms and 11-fold coordinated. Evidently, on Ir(110) the surface atoms with lower coordination are more reactive. For instance, DFT calculations show that the CO binding energy on Ir(110) is larger by 410 meV compared with Ir(111) in the low-coverage limit [75], a difference much larger than the 71 meV difference in binding energy of Gr to Ir(110) and Ir(111).

We speculate that the overall van der Waals interaction pulls Gr towards the surface such that the protruding atoms on Ir(110) start to hybridize with the Gr layer, while the recessed atoms do not. On the flat Ir(111) surface, Pauli repulsion stops the approach prior to the onset of significant hybridization of specific substrate orbitals with the Gr sheet [76]. Based on this proposed scenario, we speculate that a similar difference in binding also holds for Gr on other metal surfaces, e.g., for Pt.

#### IV. CONCLUSION

Single-crystal Gr on Ir(110) forms upon low-pressure chemical vapor deposition growth at 1500 K, displays a rectangular moiré pattern with periodicities  $m_1 = 33$  Å in the [001] direction and  $m_2 = 10$  Å in the  $[1\bar{1}0]$  direction, and can be approximated as a  $\begin{pmatrix} 8 & 4 \\ 0 & 11 \end{pmatrix}$  superstructure with respect to Ir(110). The Gr layer is chemisorbed to Ir(110) with an adsorption energy of  $-140.2$  meV per C atom. Due to strong and locally varying interaction with the substrate, it lacks a Dirac cone.

The Gr layer displays a wave pattern with wave vector in the [001] direction and corrugation of  $\approx 0.4$  Å according to our *ab initio* calculations. This wave pattern implies a modulation in charge transfer to the Gr  $\pi$  system and in the Gr-Ir hybridization, both being most pronounced in the trough of the wave pattern. The effect of this property modulation on the physisorption of aromatic molecules is explored through *ab initio* calculations for a naphthalene molecule. The adsorption energy landscape is found to be highly anisotropic with the maximum binding energy for molecules with their long axis adsorbed along the troughs, where the van der Waals interaction is strongest because of the larger transferred charge to Gr. The same property modulation is shown experimentally to enable the alignment of EuCot sandwich-molecular wires along troughs at 300 K. The successful on-surface synthesis—requiring reevaporation of excess Cot molecules and the diffusion of reaction intermediates—also

documents the inertness of the substrate. Based on these results, we speculate that Gr/Ir(110) can be used as a template in organometallic on-surface synthesis as well as for the templated adsorption of many molecular species. Being an inert 2D single-crystal substrate, we also speculate that Gr/Ir(110) can be used for the growth of quasifreestanding monolayers of 2D materials through reactive molecular beam epitaxy, similar to other inert 2D single-crystal substrates [2–5].

Under the Gr cover, Ir(110) remains unreconstructed down to the lowest temperatures. It is argued that the strong adhesion between Gr and Ir(110) suppresses the formation of the nanofacet,  $(2 \times 1)$ , and  $(3 \times 1)$  reconstructions. It remains to be explored whether this property can be used for the growth of epitaxial layers on unreconstructed Ir(110), e.g., by intercalation of metallic species at elevated temperatures.

## ACKNOWLEDGMENTS

This work was funded by the Deutsche Forschungsgemeinschaft (DFG, German Research Foundation) within the project “Sandwich molecular nanowires: on-surface synthesis, structure and magnetism” (Grants No. MI 581/23-1, No. AT 109/5-1, and No. WE 2623/17-1, Project No. 389895192). V.C., N.A., J.F., T.K., and T.M. acknowledge additional DFG support within CRC1238, Project No. 277146874 - CRC 1238 (subprojects C01 and B06). The authors gratefully acknowledge the computing time granted by the JARA Vergabegremium and provided on the JARA Partition part of the supercomputer JURECA at Forschungszentrum Jülich. This work was also supported by Villum Fonden via the Centre of Excellence for Dirac Materials (Grant No. 11744).

- 
- [1] J. Klinkhammer, D. F. Förster, S. Schumacher, H. P. Oepen, T. Michely, and C. Busse, Structure and magnetic properties of ultra thin textured EuO films on graphene, *Appl. Phys. Lett.* **103**, 131601 (2013).
- [2] M. M. Ugeda, A. J. Bradley, S.-F. Shi, F. H. da Jornada, Y. Zhang, D. Y. Qiu, W. Ruan, S.-K. Mo, Z. Hussain, Z.-X. Shen, F. Wang, S. G. Louie, and M. F. Crommie, Giant bandgap renormalization and excitonic effects in a monolayer transition metal dichalcogenide semiconductor, *Nat. Mater.* **13**, 1091 (2014).
- [3] M. M. Ugeda, A. J. Bradley, Y. Zhang, S. Onishi, Y. Chen, W. Ruan, C. Ojeda-Aristizabal, H. Ryu, M. T. Edmonds, H.-Z. Tsai, A. Riss, S.-K. Mo, D. Lee, A. Zettl, Z. Hussain, Z.-X. Shen, and M. F. Crommie, Characterization of collective ground states in single-layer NbSe<sub>2</sub>, *Nat. Phys.* **12**, 92 (2016).
- [4] J. Hall, B. Pielić, C. Murray, W. Jolie, T. Wekking, C. Busse, M. Kralj, and T. Michely, Molecular beam epitaxy of quasifreestanding transition metal disulphide monolayers on van der Waals substrates: a growth study, *2D Mater.* **5**, 025005 (2018).
- [5] C. Murray, W. Jolie, J. A. Fischer, J. Hall, C. van Efferen, N. Ehlen, A. Grüneis, C. Busse, and T. Michely, Comprehensive tunneling spectroscopy of quasifreestanding MoS<sub>2</sub> on graphene on Ir(111), *Phys. Rev. B* **99**, 115434 (2019).
- [6] M. Garnica, D. Stradi, S. Barja, F. Calleja, C. Díaz, M. Alcamí, N. Martín, A. L. Vázquez de Parga, F. Martín, and R. Miranda, Long-range magnetic order in a purely organic 2D layer adsorbed on epitaxial graphene, *Nat. Phys.* **9**, 368 (2013).
- [7] S. K. Hämäläinen, M. Stepanova, R. Drost, P. Liljeroth, J. Lahtinen, and J. Sainio, Self-assembly of cobalt-phthalocyanine molecules on epitaxial graphene on Ir(111), *J. Phys. Chem. C* **116**, 20433 (2012).
- [8] F. Huttmann, N. Schleheck, N. Atodiresei, and T. Michely, On-surface synthesis of sandwich molecular nanowires on graphene, *J. Am. Chem. Soc.* **139**, 9895 (2017).
- [9] J. Mao, H. Zhang, Y. Jiang, Y. Pan, M. Gao, W. Xiao, and H.-J. Gao, Tunability of supramolecular kagome lattices of magnetic phthalocyanines using graphene-based moiré patterns as templates, *J. Am. Chem. Soc.* **131**, 14136 (2009).
- [10] R. Baltic, M. Pivetta, F. Donati, C. Wäckerlin, A. Singha, J. Dreiser, S. Rusponi, and H. Brune, Superlattice of single atom magnets on graphene, *Nano Lett.* **16**, 7610 (2016).
- [11] T. Hartl, M. Will, D. Čapeta, R. Singh, D. Scheinecker, V. Boix de la Cruz, S. Dellmann, P. Lacovig, S. Lizzit, B. V. Senkovskiy, A. Grüneis, M. Kralj, J. Knudsen, J. Kotakoski, T. Michely, and P. Bampoulis, Cluster superlattice membranes, *ACS Nano* **14**, 13629 (2020).
- [12] V. Borovikov and A. Zangwill, Step-edge instability during epitaxial growth of graphene from SiC(0001), *Phys. Rev. B* **80**, 121406(R) (2009).
- [13] J. Kraus, S. Böcklein, R. Reichelt, S. Günther, B. Santos, T. O. Mentş, and A. Locatelli, Towards the perfect graphene membrane? – Improvement and limits during formation of high quality graphene grown on Cu-foils, *Carbon* **64**, 377 (2013).
- [14] J. Bao, O. Yasui, W. Norimatsu, K. Matsuda, and M. Kusunoki, Sequential control of step-bunching during graphene growth on SiC(0001), *Appl. Phys. Lett.* **109**, 081602 (2016).
- [15] I. Šrut Rakić, M. Kralj, W. Jolie, P. Lazić, W. Sun, J. Avila, M.-C. Asensio, F. Craes, V. M. Trontl, C. Busse, and P. Pervan, Step-induced faceting and related electronic effects for graphene on Ir(332), *Carbon* **110**, 267 (2016).
- [16] Y. S. Dedkov, M. Fonin, U. Rüdiger, and C. Laubschat, Graphene-protected iron layer on Ni(111), *Appl. Phys. Lett.* **93**, 022509 (2008).
- [17] L. Nilsson, M. Andersen, J. Bjerre, R. Balog, B. Hammer, L. Hornekær, and I. Stensgaard, Preservation of the Pt(100) surface reconstruction after growth of a continuous layer of graphene, *Surf. Sci.* **606**, 464 (2012).
- [18] L. Nilsson, M. Andersen, R. Balog, E. Lægsgaard, P. Hofmann, F. Besenbacher, B. Hammer, I. Stensgaard, and L. Hornekær, Graphene coatings: Probing the limits of the one atom thick protection layer, *ACS Nano* **6**, 10258 (2012).
- [19] M. Batzill, The surface science of graphene: Metal interfaces, CVD synthesis, nanoribbons, chemical modifications, and defects, *Surf. Sci. Rep.* **67**, 83 (2012).
- [20] S. Marchini, S. Günther, and J. Wintterlin, Scanning tunneling microscopy of graphene on Ru(0001), *Phys. Rev. B* **76**, 075429 (2007).
- [21] T. A. Land, T. Michely, R. J. Behm, J. C. Hemminger, and G. Comsa, Direct observation of surface reactions by scanning tunneling microscopy: Ethylene → ethynidyne → carbon particles → graphite on Pt(111), *J. Chem. Phys.* **97**, 6774 (1992).

- [22] L. Gao, J. R. Guest, and N. P. Guisinger, Epitaxial graphene on Cu(111), *Nano Lett.* **10**, 3512 (2010).
- [23] D. Martoccia, M. Björck, C. M. Schlepütz, T. Brugger, S. A. Pauli, B. D. Patterson, T. Greber, and P. R. Willmott, Graphene on Ru(0001): a corrugated and chiral structure, *New J. Phys.* **12**, 043028 (2010).
- [24] E. Loginova, S. Nie, K. Thürmer, N. C. Bartelt, and K. F. McCarty, Defects of graphene on Ir(111): Rotational domains and ridges, *Phys. Rev. B* **80**, 085430 (2009).
- [25] H. Hattab, A. T. N'Diaye, D. Wall, G. Jnawali, J. Coraux, C. Busse, R. van Gastel, B. Poelsema, T. Michely, F.-J. Meyer zu Heringdorf, and M. Horn-von Hoegen, Growth temperature dependent graphene alignment on Ir(111), *Appl. Phys. Lett.* **98**, 141903 (2011).
- [26] A. Fedorov, A. Varykhalov, A. Dobrotvorskii, A. Chikina, V. Adamchuk, and D. Usachov, Structure of graphene on the Ni(110) surface, *Phys. Solid State* **53**, 1952 (2011).
- [27] O. Dugerjav, G. Duvjir, L. Tapasztó, and C. Hwang, Growth of graphene on the Cu(110) surface, *J. Phys. Chem. C* **124**, 12106 (2020).
- [28] S. Achilli, E. Cavaliere, T. H. Nguyen, M. Cattelan, and S. Agnoli, Growth and electronic structure of 2D hexagonal nanosheets on a corrugated rectangular substrate, *Nanotechnology* **29**, 485201 (2018).
- [29] N. A. Vinogradov, A. A. Zakharov, V. Kocovski, J. Ruzs, K. A. Simonov, O. Eriksson, A. Mikkelsen, E. Lundgren, A. S. Vinogradov, N. Mårtensson, and A. B. Preobrajenski, Formation and Structure of Graphene Waves on Fe(110), *Phys. Rev. Lett.* **109**, 026101 (2012).
- [30] J. Dai, D. Wang, M. Zhang, T. Niu, A. Li, M. Ye, S. Qiao, G. Ding, X. Xie, Y. Wang, P. K. Chu, Q. Yuan, Z. Di, X. Wang, F. Ding, and B. I. Yakobson, How graphene islands are unidirectionally aligned on the Ge(110) surface, *Nano Lett.* **16**, 3160 (2016).
- [31] L. Bignardi, S. K. Mahatha, D. Lizzit, H. Bana, E. Travaglia, P. Lacovig, C. Sanders, A. Baraldi, P. Hofmann, and S. Lizzit, Anisotropic strain in epitaxial single-layer molybdenum disulfide on Ag(110), *Nanoscale* **13**, 18789 (2021).
- [32] J.-H. Lee, E. K. Lee, W.-J. Joo, Y. Jang, B.-S. Kim, J. Y. Lim, S.-H. Choi, S. J. Ahn, J. R. Ahn, M.-H. Park, C.-W. Yang, B. L. Choi, S.-W. Hwang, and D. Whang, Wafer-scale growth of single-crystal monolayer graphene on reusable hydrogen-terminated germanium, *Science* **344**, 286 (2014).
- [33] M. Corso, T. Greber, and J. Osterwalder, h-BN on Pd(110): a tunable system for self-assembled nanostructures? *Surf. Sci.* **577**, L78 (2005).
- [34] T. Greber, L. Brandenberger, M. Corso, A. Tamai, and J. Osterwalder, Single layer hexagonal boron nitride films on Ni(110), *e-J. Surf. Sci. Nanotechnol.* **4**, 410 (2006).
- [35] M. P. Allan, S. Berner, M. Corso, T. Greber, and J. Osterwalder, Tunable self-assembly of one-dimensional nanostructures with orthogonal directions, *Nanoscale Res. Lett.* **2**, 94 (2007).
- [36] A. J. Martínez-Galera and J. M. Gómez-Rodríguez, Influence of metal support in-plane symmetry on the corrugation of hexagonal boron nitride and graphene monolayers, *Nano Res.* **11**, 4643 (2018).
- [37] D. Steiner, F. Mittendorfer, and E. Bertel, Quasiliquid layer promotes hexagonal boron nitride (h-BN) single-domain growth: h-BN on Pt(110), *ACS Nano* **13**, 7083 (2019).
- [38] R. Koch, M. Borbonus, O. Haase, and K. H. Rieder, New Aspects on the Ir(110) Reconstruction: Surface Stabilization on Mesoscopic Scale via (331) Facets, *Phys. Rev. Lett.* **67**, 3416 (1991).
- [39] F. Huttmann, N. Rothenbach, S. Kraus, K. Ollefs, L. M. Arruda, M. Bernien, D. Thonig, A. Delin, J. Fransson, K. Kummer, N. B. Brookes, O. Eriksson, W. Kuch, T. Michely, and H. Wende, Europium cyclooctatetraene nanowire carpets: A low-dimensional, organometallic, and ferromagnetic insulator, *J. Phys. Chem. Lett.* **10**, 911 (2019).
- [40] A. T. N'Diaye, M. Engler, C. Busse, D. Wall, N. Buckanie, F.-J. M. zu Heringdorf, R. van Gastel, B. Poelsema, and T. Michely, Growth of graphene on Ir(111), *New J. Phys.* **11**, 023006 (2009).
- [41] See Supplemental Material at <http://link.aps.org/supplemental/10.1103/PhysRevB.105.165405> for further details, including Figs. S1–S7 and Table S1.
- [42] I. Horcas, R. Fernández, J. M. Gómez-Rodríguez, J. Colchero, J. Gómez-Herrero, and A. M. Baro, WSXM: A software for scanning probe microscopy and a tool for nanotechnology, *Rev. Sci. Instrum.* **78**, 013705 (2007).
- [43] P. Hohenberg and W. Kohn, Inhomogeneous electron gas, *Phys. Rev.* **136**, B864 (1964).
- [44] W. Kohn and L. J. Sham, Self-consistent equations including exchange and correlation effects, *Phys. Rev.* **140**, A1133 (1965).
- [45] P. E. Blöchl, Projector augmented-wave method, *Phys. Rev. B* **50**, 17953 (1994).
- [46] G. Kresse and J. Hafner, *Ab initio* molecular dynamics for liquid metals, *Phys. Rev. B* **47**, 558 (1993).
- [47] G. Kresse and J. Furthmüller, Efficient iterative schemes for *ab initio* total-energy calculations using a plane-wave basis set, *Phys. Rev. B* **54**, 11169 (1996).
- [48] G. Kresse and D. Joubert, From ultrasoft pseudopotentials to the projector augmented-wave method, *Phys. Rev. B* **59**, 1758 (1999).
- [49] K. Lee, E. D. Murray, L. Kong, B. I. Lundqvist, and D. C. Langreth, Higher-accuracy van der Waals density functional, *Phys. Rev. B* **82**, 081101(R) (2010).
- [50] I. Hamada, van der Waals density functional made accurate, *Phys. Rev. B* **89**, 121103(R) (2014).
- [51] A. D. Becke, On the large gradient behavior of the density functional exchange energy, *J. Chem. Phys.* **85**, 7184 (1986).
- [52] A. T. N'Diaye, J. Coraux, T. N. Plasa, C. Busse, and T. Michely, Structure of epitaxial graphene on Ir(111), *New J. Phys.* **10**, 043033 (2008).
- [53] P. Eckerlin and H. Kandler, *Group III: Condensed Matter, Landolt-Börnstein: Numerical Data and Functional Relationships in Science and Technology - New Series Vol. 6* (Springer-Verlag, Berlin, 1971), p. 626.
- [54] F. H. Farwick zum Hagen, D. M. Zimmermann, C. C. Silva, C. Schlueter, N. Atodiresei, W. Jolie, A. J. Martínez-Galera, D. Dombrowski, U. A. Schröder, M. Will, P. Lazić, V. Caciuc, S. Blügel, T.-L. Lee, T. Michely, and C. Busse, Structure and growth of hexagonal boron nitride on Ir(111), *ACS Nano* **10**, 11012 (2016).
- [55] F. Huttmann, A. J. Martínez-Galera, V. Caciuc, N. Atodiresei, S. Schumacher, S. Standop, I. Hamada, T. O. Wehling, S. Blügel, and T. Michely, Tuning the van der Waals Interaction

- of Graphene with Molecules via Doping, *Phys. Rev. Lett.* **115**, 236101 (2015).
- [56] Q. Wang, L. Wei, M. Sullivan, S.-W. Yang, and Y. Chen, Graphene layers on Cu and Ni(111) surfaces in layer controlled graphene growth, *RSC Adv.* **3**, 3046 (2013).
- [57] S. V. Hoffmann, C. Søndergaard, C. Schultz, Z. Li, and P. Hofmann, An undulator-based spherical grating monochromator beamline for angle-resolved photoemission spectroscopy, *Nucl. Instrum. Methods Phys. Res., Sect. A* **523**, 441 (2004).
- [58] Y. Dedkov and E. Voloshina, Graphene growth and properties on metal substrates, *J. Phys.: Condens. Matter* **27**, 303002 (2015).
- [59] A. Varykhalov, J. Sánchez-Barriga, D. Marchenko, P. Hlawenka, P. S. Mandal, and O. Rader, Tunable Fermi level and hedgehog spin texture in gapped graphene, *Nat. Commun.* **6**, 7610 (2015).
- [60] A. Varykhalov, D. Marchenko, J. Sánchez-Barriga, M. R. Scholz, B. Verberck, B. Trauzettel, T. O. Wehling, C. Carbone, and O. Rader, Intact Dirac Cones at Broken Sublattice Symmetry: Photoemission Study of Graphene on Ni and Co, *Phys. Rev. X* **2**, 041017 (2012).
- [61] A. Chakradhar, K. Trettel, and U. Burghaus, Benzene adsorption on Ru(0001) and graphene/Ru(0001)-how to synthesize epitaxial graphene without STM or LEED? *Chem. Phys. Lett.* **590**, 146 (2013).
- [62] N. Hosoya, R. Takegami, J.-i. Suzumura, K. Yada, K. Miyajima, M. Mitsui, M. B. Knickelbein, S. Yabushita, and A. Nakajima, Formation and electronic structures of organoeuropium sandwich nanowires, *J. Phys. Chem. A* **118**, 8298 (2014).
- [63] A. Nakajima and K. Kaya, A novel network structure of organometallic clusters in the gas phase, *J. Phys. Chem. A* **104**, 176 (2000).
- [64] N. Atodiresei, P. H. Dederichs, Y. Mokrousov, L. Bergqvist, G. Bihlmayer, and S. Blügel, Controlling the Magnetization Direction in Molecules via Their Oxidation State, *Phys. Rev. Lett.* **100**, 117207 (2008).
- [65] X. Zhang, M.-F. Ng, Y. Wang, J. Wang, and S.-W. Yang, Theoretical studies on structural, magnetic, and spintronic characteristics of sandwiched  $\text{Eu}_n\text{COT}_{n+1}$  ( $n = 1-4$ ) clusters, *ACS Nano* **3**, 2515 (2009).
- [66] K. Xu, J. Huang, S. Lei, H. Su, F. Y. C. Boey, Q. Li, and J. Yang, Efficient organometallic spin filter based on europium-cyclooctatetraene wire, *J. Chem. Phys.* **131**, 104704 (2009).
- [67] R. Shuttleworth, The surface tension of solids, *Proc. Phys. Soc. A* **63**, 444 (1950).
- [68] A. Ney, J. Schulz, M. Sturmat, and R. Koch, Stress-driven self-assembly on Ir(110): stripes, droplets, and missing-row-type reconstructions, *Surf. Sci.* **519**, 192 (2002).
- [69] J. J. Schulz, M. Sturmat, and R. Koch, Illuminating structural transformation of Ir(110): A high-temperature scanning tunneling microscopy study, *Phys. Rev. B* **62**, 15402 (2000).
- [70] I. K. Robinson, E. Vlieg, and K. Kern, Structure and roughening of the Pt(110) surface, *Faraday Discuss. Chem. Soc.* **89**, 159 (1990).
- [71] R. Tran, Z. Xu, B. Radhakrishnan, D. Winston, W. Sun, K. A. Persson, and S. P. Ong, Surface energies of elemental crystals, *Sci. Data* **3**, 160080 (2016).
- [72] K. H. Hellwege, O. Madelung, M. Schulz, and H. Weiss, *Semiconductors, Physics of Group IV Elements and III-V Compounds, Landolt-Börnstein, New Series, Group III*, Vol. 17 Part A (Springer-Verlag, Berlin, 1982).
- [73] P. L. Silvestrelli and A. Ambrosetti, van der Waals corrected DFT simulation of adsorption processes on transition-metal surfaces: Xe and graphene on Ni(111), *Phys. Rev. B* **91**, 195405 (2015).
- [74] F. Mittendorfer, A. Garhofer, J. Redinger, J. Klimeš, J. Harl, and G. Kresse, Graphene on Ni(111): Strong interaction and weak adsorption, *Phys. Rev. B* **84**, 201401(R) (2011).
- [75] C. Liu, L. Zhu, P. Ren, X. Wen, Y.-W. Li, and H. Jiao, High-coverage CO adsorption and dissociation on Ir(111), Ir(100), and Ir(110) from computations, *J. Phys. Chem. C* **123**, 6487 (2019).
- [76] C. Busse, P. Lazić, R. Djemour, J. Coraux, T. Gerber, N. Atodiresei, V. Caciuc, R. Brako, A. T. N'Diaye, S. Blügel, J. Zegenhagen, and T. Michely, Graphene on Ir(111): Physisorption with Chemical Modulation, *Phys. Rev. Lett.* **107**, 036101 (2011).